

1 **Quantification of the contribution of the Beauce**
2 **Groundwater Aquifer to the discharge of the Loire River**
3 **using thermal infrared satellite imaging**
4

5 **E. Lalot¹, F. Curie¹, V. Wawrzyniak², F. Baratelli³, S.**
6 **Schomburgk⁴, N. Flipo³, H. Piegay², F. Moatar¹**

7 [1]{ Laboratoire GEHCO, UFR sciences et techniques, Université François Rabelais, Tours,
8 France }

9 [2]{ Plateforme ISIG, CNRS-UMR 5600 EVS, Ecole Normale Supérieure de Lyon,
10 Université de Lyon, Lyon, France }

11 [3]{ Centre de Géosciences – Systèmes hydrologiques et Réservoirs, Mines ParisTech,
12 Fontainebleau, France }

13 [4]{ Dir. Eau Environnement et Ecotechnologies, Bureau de Recherches Géologiques et
14 Minières (BRGM), Orléans, France }

15 Correspondence to: E. Lalot (eric.lalot@gmail.com)

16

17 **Abstract**

18 Seven Landsat thermal infrared (TIR) images taken over the period 2000-2010 were used to
19 establish longitudinal temperature profiles of the middle Loire River where it flows above the
20 Beauce aquifer. The groundwater discharge along the River course was quantified for each
21 identified groundwater catchment area using a heat budget based on temperature variations of
22 the Loire River estimated from the TIR images. The results showed that 75% of the temperature

23 differences, between *in situ* observations and TIR image based estimations, remained within
24 the $\pm 1^{\circ}\text{C}$ interval. The main discharge area of the Beauce aquifer into the Loire River was
25 located between river kilometers 630 and 650, where there was a temperature drop of around
26 1°C to 1.5°C in the summer and a rise of about 0.5°C in winter. According to the heat budgets,
27 groundwater discharge was higher during the winter period ($13.5 \text{ m}^3.\text{s}^{-1}$) than during the
28 summer period ($5.3 \text{ m}^3.\text{s}^{-1}$). These findings are in line with the results of both a groundwater
29 budget and a process-based distributed hydrogeological model. Groundwater input was also
30 found to be higher during the Loire's flow recession periods.

31

32 **1 Introduction**

33 Water temperature is a key factor for aquatic fauna (Ward, 1992; Caissie, 2006). For instance,
34 it controls oxygen dissolution, essential for aquatic organisms. River temperature is controlled
35 by many factors such as solar radiation, air temperature or groundwater discharge (Webb and
36 Zhang, 1997, 1999; Hannah et al., 2004). However, quantifying the respective influence of
37 these factors is often difficult, since temperature profiles of the river course have first to be
38 established.

39 Since the late 1990s thermal infrared images (TIR) have been used to determine river water
40 temperature along sections ranging from tens to hundreds of kilometers (Torgersen et al., 2001;
41 Handcock et al., 2006 and 2012). Until now, these images of water courses have mainly been
42 used: i) to identify cold refuges for fish in the summer (Belknap and Naiman, 1998; Torgersen
43 et al., 1999; Tonolla et al., 2010; Monk et al., 2013); ii) to study the thermal variability of rivers
44 or alluvial floodplains and locate areas of similar thermal characteristics (Smikrud et al., 2008;
45 Tonolla et al., 2010; Wawrzyniak et al., 2012, 2013); iii) to validate river temperature models
46 (Boyd and Kasper, 2003; Cristea and Burges, 2009).

47 Most of these studies have been based on airborne TIR images, while studies based on TIR
48 satellite images are scarce, mainly due to their poor spatial resolution. In the case of the Landsat
49 7 satellite, one pixel of the TIR image represents 60*60 m on the ground. Therefore, only a few
50 large river courses can be studied using TIR satellite images, as it is usually considered that
51 river width must exceed 3 image pixels to provide an accurate estimation of water temperature
52 (Handcock et al., 2006; Wawrzyniak et al., 2012). However, the advantage of Landsat satellite
53 images over airborne images is that they are freely available at different dates, providing
54 archives to explore inter-annual or seasonal patterns. As the surface area covered by a single
55 satellite image would require a long time to be covered by air, longitudinal thermal profiles
56 derived from TIR satellite images also show less bias due to change in water temperature during
57 sampling time.

58 Groundwater discharge has already been shown to have a significant influence on surface water
59 temperature (Hannah et al., 2004; Webb and Zhang, 1997, 1999), however, this influence has
60 seldom been studied using TIR images (Loheide and Gorelick, 2006; Burkholder et al., 2007;
61 Wang et al., 2008, Danielescu et al., 2009; Mallast et al., 2014). Only one paper describes a test
62 to quantify the groundwater discharge in a small stream, based on the longitudinal temperature
63 profile established from airborne TIR images (Loheide and Gorelick, 2006). To our knowledge,
64 groundwater discharge into rivers has never been observed or quantified using satellite TIR
65 images.

66 Locating groundwater discharge areas is crucial to assess the vulnerability of aquatic fauna, as
67 these locations can act as sheltered areas (Belknap and Naiman, 1998). Understanding water
68 temperature variations along the middle Loire River, where several nuclear power plants are
69 located, is an operational issue for “Electricité De France” (EDF). For example, between the
70 nuclear power plants of Dampierre and Saint – Laurent des Eaux, the Loire River temperature

71 has been shown to be influenced by the groundwater discharge from the Beauce aquifer and the
72 Val d'Orléans hydrogeological system (Alberic and Lepiller, 1998; Alberic, 2004; Moatar and
73 Gailhard, 2006). The average discharge of the Beauce aquifer was previously quantified using
74 hydrogeological numerical modeling (Monteil, 2011; Flipo et al., 2012) and was found to have
75 an inter annual average of approximately $10 \text{ m}^3 \cdot \text{s}^{-1}$. However, until now, field measurement
76 data has not been used to accurately locate or quantify the groundwater discharge.

77 The main aims of this study were therefore to test the ability of thermal infrared images from
78 the Landsat satellite i) to accurately determine water temperature in a river with a width of less
79 than 180 m; ii) to characterize the longitudinal and temporal variations of temperature along a
80 135 km section of the middle Loire River overlying the Beauce aquifer between Dampierre and
81 Blois; iii) to locate and quantify the contribution of the Beauce aquifer groundwater discharge
82 into the Loire River.

83

84 **2 Study area**

85 The study site was the Loire River between Gien and Blois (a 135 km reach), which overlies
86 the Beauce aquifer (Figure 1). The catchment area of the Loire at Gien is $35,000 \text{ km}^2$ and the
87 river slope is $0.4 \text{ m} \cdot \text{km}^{-1}$ in the studied section (Latapie et al., 2014).

88 The river flow rate is measured daily in Gien, Orléans and Blois, respectively at river kilometers
89 560, 635 and 695 (Banque HYDRO: www.hydro.eaufrance.fr). Over the 1964 to 2011 period,
90 in Orléans the average flow rate was $345 \text{ m}^3 \cdot \text{s}^{-1}$, and the average flow rates in August and
91 January were $95 \text{ m}^3 \cdot \text{s}^{-1}$ and $553 \text{ m}^3 \cdot \text{s}^{-1}$ respectively.

92 The width of the wet section of the middle Loire River ranges between 200 m and 450 m
93 (Latapie et al., 2014), which is higher than the three image pixel threshold (180 m). However,
94 during low flow periods, the Loire River forms several branches locally and the main branch

95 width can be as low as 50 m. During these periods, the average river depth is about 1 m in the
96 studied reach. Along the Loire River, the main natural and artificial weirs are located at river
97 kilometers 571, 603, 635, 661, and 670, where the water level shows a drop of just over 1 m
98 during low flow periods.

99 The climate of the study area is temperate. The mean annual air temperature in Orléans is 11°C.
100 The cold season lasts from mid-November to early March, with an average air temperature of
101 4.0°C (data from Météo France at Orléans station for the period 1961-1990). The warm season
102 lasts from late May to early September, with an average air temperature of 17.2°C.

103 The water temperature of the Loire River is influenced by several factors: i) atmospheric heat
104 fluxes from direct solar radiation, diffuse solar radiation, latent heat exchange, conduction and
105 water emitted radiation; ii) groundwater discharge from the Beauce aquifer and Val d'Orléans
106 hydrosystem (Alberic, 2004; Gutierrez and Binet, 2010); iii) warm water originating from the
107 cooling systems of the nuclear power plants of Dampierre and Saint-Laurent des Eaux (average
108 discharge of $2 \text{ m}^3 \cdot \text{s}^{-1}$ from nuclear reactors). However, the nuclear power plants only have a
109 slight influence on the temperature of the river, as the cooling towers remove much of the heat.
110 The median temperature rise between the upstream and downstream sections of the nuclear
111 power plants is 0.1°C with a 90th percentile of 0.3°C (Bustillo et al., 2014). The greatest increase
112 in river temperature due to the power plants is observed in winter, during low flow periods
113 ($<1^\circ\text{C}$); iv) in-flows from the tributaries. The catchment area of the Loire River between Gien
114 and Blois is around 5,600 km², (a 16% increase in the catchment area over the 135 km reach).
115 The influence of the tributaries on the river temperature is considered negligible in this section,
116 since the water temperature of the tributaries is usually close to that of the Loire itself (Moatar
117 and Gailhard, 2006) and the flow rates of the tributaries is low (less than $1 \text{ m}^3 \cdot \text{s}^{-1}$). However, in
118 this section the main tributary of the Loire is the Loiret which drains water originating from

119 both the Beauce aquifer and the Loire (Alberic, 2004; Binet et al., 2011) and is very short (6
120 km). The influence of the Loiret River can therefore be included with that of the Beauce aquifer.

121

122 **3 Material and methods**

123 **3.1 Data**

124 Seven satellite images from the Landsat 7 ETM+, presenting cloud cover under 10 %, were
125 extracted from the period 1999-2010 (<http://earthexplorer.usgs.gov/>) (Table 1). Five images
126 were available in the warm season and two in the cold season. They were taken at 12h30 LT in
127 summer and 11h30 LT in winter. Each image covered the entire course of the Loire River
128 between Gien and Blois.

129 Water temperatures of the Loire River are monitored by EDF upstream of the nuclear power
130 plant of Dampierre (river kilometer 571) and Saint-Laurent des Eaux (river kilometer 670) on
131 an hourly basis. The average daily water temperature observed, on the days when the images
132 were taken, was 5.2°C in the cold season and 23.7°C in the warm season.

133 River flow rates measured in Orléans, on the days the images were taken, were between 61
134 m³.s⁻¹ and 478 m³.s⁻¹. On six out of the seven dates, the Loire River discharge/ flow rate was
135 lower than the mean annual flow.

136 **3.2 From the TIR satellite images to the longitudinal temperature profiles of** 137 **the Loire River**

138 The first step was to locate pixels corresponding to water only. To this end, a threshold based
139 on the TM 8 band of the Landsat images (0.52 to 0.9 μm; USGS, 2013) was used and only
140 values below the threshold were kept. The aerial images in the visible range from the Ortho
141 database, of the “Institut National de l’information Géographique et forestière” (IGN), were

142 used to set the threshold value for each image by comparing the TM 8 band to the Loire water
143 course in known locations and where it did not alter with time. The Carthage database from the
144 IGN, which maps all the French watercourses as lines, enabled the water pixels belonging to
145 the Loire River to be separated from those belonging to other water bodies. As shade resulting
146 from the clouds merges with the water pixel, it was removed manually using the same TM 8
147 band. The main advantage of using the TM8 band to detect water is that its spatial resolution
148 (15 m) is much higher than that of the TM 61 band (60 m resolution, subsampled at 30 m; 10.4
149 to 12.5 μm) which is used to estimate water temperature.

150 A previous study (Handcock et al. 2006), demonstrated that river temperatures should be
151 estimated using only pure water pixels (i.e. separated from the river banks by at least another
152 water pixel). However, in the case of the middle Loire River, pure water pixels could not be
153 found along the entire river course, especially at low flow rates. Therefore, all water pixels were
154 kept. Pixels composed of land and water were considered as land pixels.

155 In order to detect the water pixels from the TM 61 infrared band, a neighborhood analysis was
156 therefore conducted, based on the water and land pixels already identified from the TM 8 band.
157 Only pixels from the TM 61 band situated further than 60 m away from the already identified
158 land pixels (using the TM 8 band) were kept. To detect pure water pixels, a 120 m buffer zone
159 was used.

160 The temperature was then calculated for these identified Loire pixels from the radiance values
161 extracted from the TM61 band of the Landsat images using Planck's law (Chander et al., 2009).
162 A value of 0.98 was used for water emissivity. No atmospheric correction was taken into
163 account, since the study area was included in a single LANDSAT image and atmospheric
164 conditions were homogeneous within the study area (with less than 10% of cloud cover).
165 Finally, temperature values for these pixels were projected orthogonally on the longitudinal

166 profile of the Loire extracted from the Carthage database. The average temperature for 200m
167 long sections was then calculated. A distance of 200 m was chosen to be similar to the width of
168 the Loire River. After this, a moving average for 10 consecutive temperature values along the
169 water course (2 km) was calculated to smooth the temperature profile.

170 The temperature profiles extracted from the TIR images were then exploited in two different
171 ways: i) the accuracy and uncertainty of the temperatures estimated from the TIR images was
172 tested by comparing them with the hourly *in situ* measurements conducted by EDF at Dampierre
173 and Saint-Laurent des Eaux; ii) a heat budget method, based on the temperature estimated from
174 the TIR images, was used along successive sections of the Loire River to quantify the
175 groundwater discharge for each section. The results were then compared with the groundwater
176 discharge calculated using a deterministic process-based groundwater model applied over the
177 whole Loire River basin. Calculated groundwater discharge estimations were compared over
178 successive groundwater catchment areas along the Loire River.

179 **3.3 Groundwater discharge estimation - Heat budget based on TIR images**

180 The middle Loire River was divided into 11 sections, so that for each section there was only
181 one groundwater catchment area on each side of the river. The groundwater catchment areas
182 were delineated using available piezometric maps, or elevation data (surface water catchment
183 area) when the maps were missing. A description of the method can be found in Schomburgk
184 et al. (2012). The first section begins at river kilometer 560 where the flow rate is measured
185 (Gien). The groundwater discharge was estimated on each section using a heat budget based on
186 the temperatures derived from the TIR images.

187 The heat budget equilibrium can be written as (Moatar and Gailhard, 2006):

188 $\rho \cdot C \cdot Q_{i-1} \cdot T_{i-1} + F_{net} \cdot S + \rho \cdot C \cdot Q_{gw} \cdot T_{gw} = \rho \cdot C \cdot Q_i \cdot T_i$ (1)

189 $Q_{i-1} + Q_{gw} = Q_i$ (2)

190 The groundwater discharge in the section (Q_{gw}) can be deduced:

191
$$\frac{\rho \cdot C \cdot Q_{i-1} \cdot (T_{i-1} - T_i) + F_{net} \cdot S}{\rho \cdot C \cdot (T_i - T_{gw})} = Q_{gw}$$
 (3)

192 Q_{i-1} [$\text{m}^3 \cdot \text{s}^{-1}$] is the upstream flow rate of the section at temperature T_{i-1} [$^{\circ}\text{C}$], Q_i [$\text{m}^3 \cdot \text{s}^{-1}$] is the
 193 downstream flow rate of the section at temperature T_i [$^{\circ}\text{C}$]. Q_{gw} [$\text{m}^3 \cdot \text{s}^{-1}$] is the groundwater
 194 flow rate at temperature T_{gw} [$^{\circ}\text{C}$]. For each section, the flow entering the section is equal to the
 195 flow entering the previous section plus the groundwater discharge estimated over the previous
 196 section (only taken into account if the estimated discharge was positive). The groundwater
 197 temperature was considered to be 12.6°C in summer and 12.1°C in winter, based on 292
 198 measurements from the ADES database (www.ades.eaufrance.fr) conducted in the vicinity of
 199 the Loire River, over the 1991-2011 period. Over 80% of the temperature measurements were
 200 included in the interval mean plus or minus 1.4°C . F_{net} [$\text{W} \cdot \text{m}^{-2}$] stands for the atmospheric heat
 201 flux and S [m^2] is the surface area covered by the Loire River on the section. S was estimated
 202 for each section by adding the surface areas of all the water pixels identified on the satellite
 203 images from the TM 61 band. This value was therefore somewhat underestimated, as image
 204 pixels composed of both water and land were not included. ρ is the water density [$\text{kg} \cdot \text{m}^{-3}$] and
 205 C [$\text{J} \cdot \text{kg}^{-1} \cdot \text{K}^{-1}$] is the specific heat of water.

206 The heat flux (F_{net}) between the Loire River and the atmosphere was estimated as follows
 207 (Salencon and Thébault, 1997; Chapra, 1997; Table 2):

208 $F_{net} = RA + RS - RE - CV - CE$ (4)

209 Where RA is atmospheric radiation, RS solar radiation, RE emitted radiation, CV the
210 conduction and CE the condensation/evaporation.

211 The atmospheric parameters extracted from the SAFRAN database from Météo France
212 (Quintana-Segui et al., 2008) were averaged along the successive Loire River sections. All the
213 atmospheric factors were averaged over the 24 h period preceding the acquisition of the infrared
214 image. This choice is questionable as the water temperature in the Loire River may be
215 influenced by changes in atmospheric factors over a longer time period. However, the travel
216 time of water between Gien and Blois was between 1 to 1.5 days on the dates when the images
217 were taken. Atmospheric parameters were therefore not integrated over a period exceeding a
218 day.

219 As the Loire River course is wide, no shading from the alluvial forest was taken into account.

220 **3.4 Groundwater discharge estimation – Groundwater modeling**

221 The Eau-Dyssée model was used to determine the groundwater discharge along the Loire River.
222 Eau-Dyssée is an integrated, distributed, process-based model that allows the simulation of the
223 main components of the water cycle in a hydrosystem. Detailed descriptions of the model can
224 be found in Flipo et al. (2012) and Saleh et al. (2011). This model has been applied to basins of
225 different scales and hydrogeological settings, e.g., the Oise basin (4,000 km²; Saleh et al., 2011),
226 the Rhône basin (86,500 km²; Habets et al., 1999; Etchevers et al., 2001), the Seine basin
227 (65,000 km²; Ledoux et al., 2007; Pryet et al., 2015) and the Loire basin (120,000 km²; Monteil,
228 2011).

229 Eau-Dyssée divides a hydrosystem conceptually into three interacting compartments: a surface,
230 an unsaturated zone and a saturated zone. Specifically, the model couples different modules,

231 which simulate the mass balance of surface water, the runoff, the river flow rate, the fluctuations
232 of in-stream water levels, the flow rate in the unsaturated and saturated zones.

233 The water flux q_{sa} [$\text{m}^3 \cdot \text{s}^{-1}$] at the stream-aquifer interface is computed using a conductance
234 model, i.e., it is proportional to the difference between the piezometric head, h_g [m], and the
235 in-stream water level, h_r [m], i.e.:

$$236 \quad q_{sa} = k_{riv}(h_g - h_r) \quad (5)$$

237 Where the proportionality constant k_{riv} [$\text{m}^2 \cdot \text{s}^{-1}$] is the conductance of the stream-aquifer
238 interface. Rushton (2007) showed that the main factor controlling this coefficient is the
239 horizontal hydraulic conductivity k_H [$\text{m} \cdot \text{s}^{-1}$] of the underlying aquifer.

$$240 \quad k_{riv} = f k_H L \quad (6)$$

241 Where f [-] is an adjustable correction factor, generally ranging between 0.9 and 1.2 (Rushton,
242 2007), and L [m] is the length of the river in the aquifer mesh.

243 Eau-Dyssée was applied to the Loire basin by Monteil (2011). In-stream water levels were
244 assumed to be constant. This work has been improved by simulating the time variability of in-
245 stream water levels with a Manning-Strickler approach (Chow, 1959). Under the assumptions
246 that the river section is rectangular and that its width is much greater than its depth, h_r is given
247 by:

$$248 \quad h_r = b + \left(\frac{Q}{\alpha \kappa W S^{1/2}} \right)^{5/3} \quad (7)$$

249 Where b [m] is the riverbed elevation, Q [$\text{m}^3 \cdot \text{s}^{-1}$] is the discharge, $\alpha = 1 \text{ m}^{1/3} \cdot \text{s}^{-1}$, κ [-] is the
250 Strickler's coefficient, W [m] is the river width, S [-] is the slope of the riverbed.

251 Details on the input data and model calibration can be found in Monteil (2011). The
252 morphological parameters of the Loire River (river width and riverbed elevation and slope)

253 were estimated from several cross sections surveyed with an average spacing of 1.6 km (Latapie
 254 et al., 2014). The Strickler's coefficient was calibrated against observed hydrographs at six
 255 stations along the Loire River, three of which are located on the Beauce aquifer.

256 The stream-aquifer exchanges were simulated in the period 1996-2013 at a daily time step for
 257 the river network at a 1 km resolution. Groundwater discharge was then calculated for the 11
 258 Loire River sections selected for the heat budget.

259 **3.5 Uncertainty estimation – Heat budget**

260 Equation (3) was used to estimate the uncertainty associated with the calculated groundwater
 261 discharge. The absolute uncertainty of the calculated groundwater discharge ΔQ_{gw} can be
 262 computed as:

$$\begin{aligned}
 263 \quad \Delta Q_{gw} = & \left| \frac{\rho.C.(T_{i-1}-T_i)}{\rho.C.(T_i-T_{gw})} \right| \cdot \Delta Q_{i-1} + \left| \frac{\rho.C.Q_{i-1}}{\rho.C.(T_i-T_{gw})} \right| \cdot \Delta(T_{i-1} - T_i) + \left| \frac{F_{net}}{\rho.C.(T_i-T_{gw})} \right| \cdot \Delta S + \\
 264 \quad & \left| \frac{(\rho.C.Q_{i-1} \cdot (T_{i-1}-T_i) + F_{net} \cdot S)}{\rho.C.(T_i-T_{gw})^2} \right| \cdot \Delta(T_i - T_{gw}) \quad (8)
 \end{aligned}$$

265 ΔQ_{i-1} is the absolute uncertainty in the river flow rate. A 10% uncertainty in the flow estimation
 266 is considered: $\Delta Q_{i-1} = 0.1 \cdot Q_{i-1}$ (9)

267 $\Delta(T_{i-1} - T_i)$ is the absolute uncertainty in the river temperature variations over the
 268 corresponding river section. It is computed, based on the known spatial variation between
 269 Dampierre and Saint-Laurent des Eaux of the difference between the temperature estimated
 270 from the TIR images and that estimated from in-situ measurements. At each date, a difference
 271 by river kilometer and then by river section was calculated. The value of this difference was
 272 added to T_i to estimate the variation in surface water temperature that could be caused by
 273 uncertainties in the measurements: $(T_{i_{new}} - T_i)$.

$$274 \quad \Delta(T_{i-1} - T_i) = |(T_{i-1} - T_{i_{new}}) - (T_{i-1} - T_i)| \quad (10)$$

275 ΔS is the absolute uncertainty in the water surface estimate. It was computed based on the
276 difference between the water surface estimated from the TM 61 band and from the TM 8 band
277 of the Landsat satellite. ΔS was calculated at each date for every study section of the Loire (11
278 sections).

279 $\Delta(T_i - T_{gw})$ is the absolute uncertainty of the difference between the river temperature and the
280 groundwater temperature. It was considered to be equal to 2°C in order to take into account
281 both groundwater temperature variability and surface water temperature accuracy.

282

283 4 Results

284 4.1 Temperature accuracy and temperature uncertainty

285 Temperature accuracy is the average difference between the temperature estimated from the
286 TIR images and the temperature measured in-situ (Handcock et al., 2012). The comparison
287 between the in situ and TIR derived temperatures shows that, on average, the TIR images tend
288 to overestimate the Loire River water temperature in winter (+ 0.3°C) and to underestimate it
289 in summer (- 1°C). Over 75% of the TIR derived temperatures were between $\pm 1^\circ\text{C}$ of the
290 temperature measured directly in the river (11 times out of 14: Figure 2). However, the
291 temperature difference exceeded 1.5°C on 29/05/2003 and on 29/07/2002 at the Dampierre
292 station and on 29/07/2002 at Saint-Laurent des Eaux.

293 Temperature uncertainty can be linked to the repeatability of the measurement (Handcock et
294 al., 2012). The study of the longitudinal changes of the difference between TIR image based
295 temperature and in-situ measurements may give an idea of the degree of uncertainty (Figure 2).
296 On average, the variation in temperature difference remained below 0.8°C over the 100 km
297 reach from Dampierre to Saint-Laurent-des-Eaux, except on the 29/07/ 2002 (1.3°C) and on the

298 29/05/2003 (2.3°C). The variation of the temperature difference was between 0.0004°C.km⁻¹
299 and 0.02°C.km⁻¹ (mean of 0.007°C.km⁻¹).

300 Tests were carried out to assess the influence of the nature of the water pixels (pure or non-
301 pure) on the estimated temperature. For the 200m long sections of the Loire River where pure
302 water pixels exist, temperature was estimated for both pure and non-pure water pixels. A linear
303 regression was conducted for the temperature estimated with pure water pixels and that
304 estimated with non-pure water pixels. Taking into account the data from all the dates, the slope
305 of the regression line is 1, while it is 0.98 when summer alone is considered and 0.72 for winter
306 alone (Figure 3a; Figure 3b). The difference between the temperatures estimated from pure and
307 non-pure water pixels generally remained in the $\pm 0.5^\circ\text{C}$ interval (over 98% of the time), which
308 corresponds to the approximate resolution of the satellite sensors. Therefore, taking into account
309 non-pure water pixels does not seem to cause a large bias in the case of the Loire River.

310 However, when the number of water pixels in a 200m section of the Loire River decreases due
311 to the river being narrower the standard deviation of the observed temperature increases notably
312 (Table 3). Peak temperature values along the longitudinal temperature profile may therefore
313 appear in places where the main river branch is particularly narrow. This phenomenon is mostly
314 due to the uncertainties inherent in the satellite sensor. Uncertainty can be reduced by averaging
315 and as the number of pixels considered over a section increases the uncertainty decreases. The
316 moving average over ± 2 km which was applied to the data was therefore useful in reducing the
317 uncertainty.

318 **4.2 Longitudinal temperature profiles**

319 Among the seven longitudinal temperature profiles, three main profile types can be observed:
320 two in summer and one in winter.

321 In summer, a mean decrease in the temperature between 0.8°C and 1.5°C can be observed on
322 all the profiles between river kilometers 620 and 650. A local temperature minimum is observed
323 on every profile at river kilometer 645, close to La Chapelle-Saint-Mesmin. The temperature
324 increased again from river kilometer 660 to 680 and then remained constant or decreased once
325 more after river kilometer 680.

326 However, the temperature profiles differ between river kilometers 560 and 620, since the water
327 temperature either increased (29/05/2003 and 19/07/2010; Figure 4b) or decreased (24/08/2000,
328 29/07/2002 and 20/08/2010; Figure 3b). Another difference appears between river kilometers
329 650 and 660, with either a temperature drop (29/05/2003 and 19/07/2010) or a temperature rise
330 (29/07/2002). Then, from river kilometers 680 to 700 the temperature dropped downstream of
331 river kilometer 690 (29/05/2003, 19/07/2010 and 20/08/2010), or upstream of river kilometer
332 690 (24/08/2000 and 29/07/2002) and then was followed by a rise in the temperature.

333 In winter the temperature tended to increase sharply by around 0.5°C between river kilometers
334 630 and 650 (Figure 4a).

335 Sharp temperature changes in the longitudinal profile need to be compared with the uncertainty
336 and not with the accuracy. The sharpest temperature changes observed on the longitudinal
337 profiles were between 0.04°C.km⁻¹ and 0.1°C.km⁻¹ (mean of 0.074°C.km⁻¹). The most marked
338 temperature changes are therefore at least one order of magnitude higher than those expected
339 from the uncertainty (0.0072°C.km⁻¹). They are therefore likely to be meaningful in terms of
340 physical processes.

341 **4.3 Groundwater discharge estimation - Heat budget and groundwater** 342 **modeling**

343 The groundwater discharge was estimated at seven dates (winter and summer) along the same
344 successive 11 sections of the Loire, using both heat budget and groundwater modeling (Figure

345 5a). The variability of the groundwater discharge estimated with the heat budget was much
346 higher than that estimated using groundwater modeling (with maximum standards deviations
347 of $0.6 \text{ m}^3 \cdot \text{s}^{-1} \cdot \text{km}^{-1}$ and $0.11 \text{ m}^3 \cdot \text{s}^{-1} \cdot \text{km}^{-1}$ respectively). Nevertheless, the modeled groundwater
348 discharge was always within the interval estimated by the heat budget. Overall, compared to
349 groundwater modeling, the heat budget tended to overestimate the groundwater discharge
350 between river kilometers 640 and 660 in winter and to underestimate it between river kilometers
351 660 and 680 in summer (Figure 5b; Figure 6a; Figure 6b).

352 High groundwater discharge rates ($0.31 \text{ m}^3 \cdot \text{s}^{-1} \cdot \text{km}^{-1}$ on average) were calculated with the heat
353 budget method between river kilometers 563 and 565 and they also showed a noticeable
354 increase in the standard deviation ($0.6 \text{ m}^3 \cdot \text{s}^{-1} \cdot \text{km}^{-1}$). However, these high discharge rates and
355 high standard deviation were not observed using groundwater modeling.

356 Between river kilometers 570 and 630, the average estimated groundwater discharge using both
357 methods is low (less than $0.3 \text{ m}^3 \cdot \text{s}^{-1} \cdot \text{km}^{-1}$ and $0.1 \text{ m}^3 \cdot \text{s}^{-1} \cdot \text{km}^{-1}$ respectively) and the standard
358 deviation was also low (less than $0.4 \text{ m}^3 \cdot \text{s}^{-1} \cdot \text{km}^{-1}$ and $0.05 \text{ m}^3 \cdot \text{s}^{-1} \cdot \text{km}^{-1}$ respectively).

359 Further downstream, according to both methods, the groundwater discharge showed a marked
360 peak in the section located between river kilometers 630 and 660. At river kilometer 640, the
361 groundwater discharge estimated with the heat budget was positive at each date (between 0.3
362 and $1.5 \text{ m}^3 \cdot \text{s}^{-1} \cdot \text{km}^{-1}$) and it also corresponded to where the groundwater discharge was maximal
363 according to groundwater modeling (between 0.6 and $0.9 \text{ m}^3 \cdot \text{s}^{-1} \cdot \text{km}^{-1}$). Both methods showed a
364 high standard deviation of the groundwater discharge (0.4 and $0.1 \text{ m}^3 \cdot \text{s}^{-1} \cdot \text{km}^{-1}$ respectively).

365 For river kilometers 660 to 680 the results of the two methods were different, with a negative
366 discharge estimated by the heat budget ($-0.24 \text{ m}^3 \cdot \text{s}^{-1} \cdot \text{km}^{-1}$ on average) and a positive discharge
367 calculated by groundwater modeling ($0.12 \text{ m}^3 \cdot \text{s}^{-1} \cdot \text{km}^{-1}$ on average).

368 Negative flow values were estimated using the heat budget method. Theoretically, the estimated
369 groundwater discharge should not be negative. However, in summer, negative discharge values
370 are computed when water temperature increases but when this increase cannot be explained by
371 atmospheric heat flux. In winter, negative discharge values can also be obtained when water
372 temperature shows a decrease that cannot be explained by atmospheric heat flux.

373 The absolute uncertainty in the groundwater discharge estimated by the heat budget remained
374 below $0.4 \text{ m}^3 \cdot \text{s}^{-1} \cdot \text{km}^{-1}$ for more than 75% of the time. Taking into account the uncertainty, in
375 the Loire River section between river kilometers 636 and 645 at all the dates the estimated
376 groundwater discharge was always above $0.03 \text{ m}^3 \cdot \text{s}^{-1} \cdot \text{km}^{-1}$ and was therefore significant. On
377 this river section, the groundwater discharge estimated with the heat budget was between 2.8
378 $\text{m}^3 \cdot \text{s}^{-1}$ and $13.7 \text{ m}^3 \cdot \text{s}^{-1}$, while that estimated using groundwater modeling varied between 5.2
379 $\text{m}^3 \cdot \text{s}^{-1}$ and $8.6 \text{ m}^3 \cdot \text{s}^{-1}$.

380

381 **5 Discussion**

382 **5.1 Temperature accuracy and uncertainty**

383 There are many factors that can contribute to the accuracy or the uncertainty of the temperature
384 estimation using TIR satellite images. The main factors are the satellite sensors, the atmospheric
385 influence on the transmitted radiation (Kay et al., 2005; Chander et al., 2009; Lamaro et al.,
386 2013), the change in water emissivity with time and along the water course, the existing
387 correlation between radiation estimated at neighboring pixels (Handcock et al., 2006) and the
388 thermal stratification of water temperature (Robinson et al., 1984; Cardenas et al., 2008). The
389 TIR images only measure the temperature of the upper $100 \mu\text{m}$ of the water body (skin layer),
390 which may differ from the temperature of the entire water body (Torgersen et al., 2001).

391 The average difference between the temperature estimated from the TIR satellite images and
392 the temperature observed *in situ* was -0.51°C . On average, it is found that temperature
393 estimated using TIR images tends to underestimate real water temperature. However, the
394 opposite has also been regularly observed. Wawrzyniak et al. (2012) found that TIR images
395 overestimated the Rhône River temperature by $+0.5^{\circ}\text{C}$ on average. Another study was
396 conducted over several water courses of the Pacific Northwest rivers of the United-States
397 (Handcok et al., 2006). A mean temperature difference of $+1.2^{\circ}\text{C}$ was found, when the water
398 course width was over three image pixels and of $+2.2^{\circ}\text{C}$ when the width was between 1 and 3
399 pixels. Mean temperature differences of between $+1^{\circ}\text{C}$ and $+1.9^{\circ}\text{C}$ were found in four other
400 Pacific Northwest rivers (Cherkauer et al., 2005).

401 Negative biases were also found (Barsi et al., 2003). In the case of Lake Tahoe, the temperature
402 estimated with TIR images was on average 1.5°C to 2.5°C colder than the temperature observed
403 *in situ*. Similar results were observed on the Wenatchee River in the United States (Cristea and
404 Burges, 2009).

405 Satellite based TIR images can therefore lead to either under- or over-estimation of the water
406 temperature. Depending on the time of the year, this difference can be either positive or negative
407 (Lamaro et al., 2013, De Boer, 2014). Findings from this study confirm that water temperature
408 can be either over- or under-estimated using TIR images (Figure 2). The biggest disparity was
409 observed on the 29/07/2002, when the water temperature was maximum ($> 26^{\circ}\text{C}$) and the flow
410 rate minimum ($60 \text{ m}^3\cdot\text{s}^{-1} - 1.33 \text{ l}\cdot\text{s}^{-1}\cdot\text{km}^{-2}$). One possible explanation of this would be that
411 high evaporation at this date led to a low temperature of surface water.

412 The average temperature difference between TIR images and *in situ* measurements was similar
413 to that observed in previous studies (Handcock et al., 2006; Wawrzyniak et al., 2012), even
414 though in this study non-pure water pixels were included and no atmospheric correction was

415 applied. Temperature estimation using non-pure water pixels from TIR images may therefore
416 be more robust than previously considered. However, this study also shows that differences
417 between temperatures estimated using TIR images and temperatures observed *in situ* may
418 locally exceed 2°C.

419 The temperature estimated for non-pure water pixels could be influenced by the temperature of
420 the riverbanks. However, tests carried out show that the difference in temperatures estimated
421 using TIR images or measured *in situ* cannot be explained only by the bias resulting from the
422 use of the non-pure water pixels. Uncertainty resulting from the satellite sensors low resolution
423 can also play a role, particularly in narrow parts of the Loire.

424 **5.2 Longitudinal temperature profiles and groundwater discharge estimations**

425 TIR images of water courses have been used in the past to detect groundwater discharge areas
426 and to differentiate them from hyporheic upwelling areas (Burkholder et al., 2007). The surface
427 of the cold water plumes associated with groundwater upwelling has been shown to be
428 correlated with the groundwater discharge rate (Danielescu et al., 2009). However, quantifying
429 groundwater discharge using a river heat budget based on TIR images has only been done once,
430 on a small stream (along a 1.7 km reach, with a flow of 10 l.s⁻¹) and using high precision aerial
431 images (Loheide and Gorelick, 2006).

432 This work is new because firstly, groundwater discharge was estimated on a large river, through
433 TIR satellite images and secondly the results were compared with estimations obtained using
434 groundwater modeling. Loheide and Gorelick (2006), on the other hand, compared their
435 findings with groundwater discharge estimated through measurements of the stream flow over
436 successive stream cross sections. This last technique is difficult to use for large rivers and
437 limited section lengths, due to the high uncertainty in flow rate measurements (up to 20 %).

438 There are several sources of uncertainty in groundwater discharge estimation using the heat
439 budget. First, there is an uncertainty in the estimation of water temperature at the river surface
440 and of the river flow rate. In general in the present study, the resulting uncertainty in
441 groundwater discharge estimate remained below $0.4 \text{ m}^3 \cdot \text{s}^{-1} \cdot \text{km}^{-1}$, which is quite high in case of
442 low groundwater discharge. There are also uncertainties inherent in the heat budget method
443 used as factors such as bed friction, heat conduction through the river bed, or hyporheic
444 exchange are not included. However, for the type of slow flowing river studied, the influence
445 of bed friction is assumed to be low, particularly in summer (Evans et al., 1998). Similarly, heat
446 conduction through the bed usually plays a minor role in the overall river heat budget (Hannah
447 et al., 2008). The effect of heat conduction and hyporheic flows can be confused with the
448 groundwater discharge, which probably leads to a small overestimation of the groundwater
449 discharge. The time for water to travel along the river is not taken into account in the heat
450 budget either. As a result the river temperature tends to be slightly overestimated due to the
451 influence of the local atmospheric conditions. There are also uncertainties linked to using
452 groundwater modeling to calculate the groundwater discharge. Nevertheless, the modeling of
453 the Loire River flow in Blois, Orléans and Gien over the 1996-2013 period provided good
454 results (Nash criteria of 0.98, correlation of 0.99 and relative bias of $0.01 \text{ m}^3 \cdot \text{s}^{-1}$). Despite all
455 the uncertainties, the groundwater discharge estimated using the heat budget remained within
456 the same order of magnitude as that calculated using groundwater modeling. It was always
457 below $\pm 1 \text{ m}^3 \cdot \text{s}^{-1} \cdot \text{km}^{-1}$ of the discharge calculated using groundwater modeling. The average
458 groundwater discharge calculated using groundwater modeling was always within the range of
459 variation of the discharge estimated using the river heat budget. The shapes of the average
460 estimated groundwater discharge curve provided by the two methods are also relatively similar
461 (coefficient of determination $r^2 = 0.7$).

462 On the upstream part of the Loire, i.e. from river kilometer 560 to 635, the groundwater
463 discharge estimated from the heat budget was low (less than $0.3 \text{ m}^3 \cdot \text{s}^{-1} \cdot \text{km}^{-1}$; Figure 5a), except
464 for some dates around river kilometer 564. This is possibly explained by the fact that the Loire
465 River loses water through the Val d'Orléans karstic system between river kilometers 610 and
466 625 (Alberic, 2004; Binet et al., 2011). This is also in line with the results from the groundwater
467 modeling. The high standard deviation of the estimated discharge near river kilometer 564 could
468 be explained by both real variations in the discharge rate and the bias resulting from the small
469 length of the corresponding section. Similarly, high groundwater discharge around river
470 kilometer 564 ($0.6 \text{ m}^3 \cdot \text{s}^{-1} \cdot \text{km}^{-1}$) was also found by the BRGM, using groundwater budget over
471 the successive groundwater catchment areas to calculate the average interannual groundwater
472 discharge over the period 1998-2007 (Schomburgk et al., 2012).

473 A first thermal anomaly appears downstream of river kilometer 620. From river kilometer 636
474 to river kilometer 645 the groundwater discharge estimated with the heat budget was between
475 0.3 and $1.5 \text{ m}^3 \cdot \text{s}^{-1} \cdot \text{km}^{-1}$. Taking into account the uncertainties, the groundwater discharge
476 calculated through the heat budget always remained positive between river kilometers 636 and
477 645. This river section corresponds to a known discharge area of the Beauce aquifer and the
478 Val d'Orléans hydrosystem (Desprez and Martin, 1976; Gonzalez, 1991; Binet et al., 2011)
479 which is also identified by groundwater modeling (calculated discharge was between 0.6 and
480 $0.9 \text{ m}^3 \cdot \text{s}^{-1} \cdot \text{km}^{-1}$). Schomburgk et al. (2012) calculated a slightly lower but still significant
481 groundwater discharge of $0.5 \text{ m}^3 \cdot \text{s}^{-1} \cdot \text{km}^{-1}$. It is interesting to note that along the Loire River, the
482 maximum estimated exchange rates occurred at times when the river flow decreased over two
483 consecutive days, while the lowest exchange rate was estimated when the flow increased
484 (Figure 7). The maximum groundwater discharge was also estimated in winter ($13.5 \text{ m}^3 \cdot \text{s}^{-1}$
485 compared to $5.3 \text{ m}^3 \cdot \text{s}^{-1}$ in summer), when the groundwater level was at its highest. This is in
486 line with the results from the groundwater modeling which show an average discharge of 7.6

487 $\text{m}^3.\text{s}^{-1}$ in winter and $6 \text{ m}^3.\text{s}^{-1}$ in summer. It is known that temporal changes in river water levels
488 can lead to large modifications in exchange rates and directions (Sophocleous, 2002). During a
489 rise in the water level, water can flow into the lateral aquifer while the opposite is true during
490 low flow rates. Thus, the variation in estimated exchange rates is likely to have a physical basis.
491 An exchange rate of 11.5 to $12.5 \text{ m}^3.\text{s}^{-1}$ was calculated at la Chapelle Saint-Mesmin (river
492 kilometer 642), using geo-chemical tracers during the summer of 1986 (Gonzalez, 1991). This
493 was higher than the maximum groundwater discharge estimated in the summer using the heat
494 budget ($7.5 \text{ m}^3.\text{s}^{-1}$). Therefore, the high discharge rates estimated using the heat budget are
495 plausible. The TIR satellite images enable the main groundwater discharge area to be located
496 precisely, along the right bank of the Loire River and two to three kilometers upstream of the
497 confluence with the Loiret (Figure 8).

498 On the downstream part of the Loire River, between river kilometers 650 and 680, both heat
499 budget and groundwater modeling estimations showed a decrease in groundwater discharge.
500 Over the last 20 km downstream the heat budget would suggest a slight increase in groundwater
501 discharge, in line with the findings from Schomburgk et al. (2012). On the other hand,
502 groundwater modeling predicts a slight decrease in groundwater discharge.

503 The change in the groundwater discharge rate over time could explain why the river temperature
504 either increased or decreased between river kilometers 645 and 665, or between river kilometers
505 570 and 620. However, atmospheric factors are also likely to play a role, even though the
506 atmospheric data available do not offer a satisfactory explanation for this phenomenon. The
507 influence of warm water discharged from the nuclear power plant on the longitudinal
508 temperature profile was not noticeable either, as no sudden temperature rise was observed at
509 the locations of the nuclear plants. In the case of Saint-Laurent des Eaux, discharged warm
510 water may nevertheless contribute to a certain extent to the overall temperature rise observed

511 between river kilometers 670 and 680 (Figure 4a; Figure 4b), however, the temperature rise
512 began upstream of the power plant.

513 Similarly, no sudden temperature variations could be explained by weirs across the river course
514 or changes in the river slope (less than 0.1°C change between a kilometer up- or downstream
515 of the structure), although abrupt temperature changes near weirs have been observed on the
516 Ain River in France (Wawrzyniak, 2012), based on airborne TIR images. This could be
517 explained by the small reservoir capacity of the Loire River upstream of the weirs (Casado et
518 al., 2013), and also due to the low spatial resolution of the TIR satellite images. The Landsat
519 images were taken around 12:30 LT and thermal stratification could be expected to be greater
520 later in the day.

521

522 **6 Conclusion**

523 Temperatures of the middle Loire River were estimated using Thermal InfraRed (TIR) Landsat
524 images. Although no atmospheric correction was implemented and non-pure water pixels were
525 taken into account, temperature differences from *in situ* observations and TIR-image based
526 estimations remain within the interval defined in previous studies (i.e. 75% of these differences
527 being in the $\pm 1^\circ\text{C}$ interval). Therefore, this study shows that river temperature may be studied
528 from TIR satellite images even when the river width falls below the three-pixel width threshold
529 (i.e. < 180 m). However, the river temperature can be seriously underestimated at low flow rates
530 and high water temperatures (differences of over 2°C).

531 We demonstrate that groundwater discharge to a large river can be estimated using satellite
532 images. The groundwater discharge was estimated along the Loire River using both the heat
533 budget based on the longitudinal temperature profiles established from the TIR images, and a
534 groundwater model. The variations of the groundwater discharge rate along the Loire River

535 were similar with both methods. The main discharge area of the Beauce aquifer into the Loire
536 River is located between river kilometers 636-645 (close to la Chapelle Saint-Mesmin).

537 According to the TIR images, the average groundwater discharge between river kilometers 636
538 and 645 appears to be higher in winter than in summer ($13.5 \text{ m}^3 \cdot \text{s}^{-1}$ and $5.3 \text{ m}^3 \cdot \text{s}^{-1}$ respectively).
539 This is in line with the results from the groundwater modeling which show an average discharge
540 of $7.6 \text{ m}^3 \cdot \text{s}^{-1}$ in winter and $6 \text{ m}^3 \cdot \text{s}^{-1}$ in summer. The groundwater discharge was also higher when
541 the river flow decreased over two consecutive days. Our TIR images highlight that
542 instantaneous groundwater discharge can vary considerably over time. Therefore, average
543 discharge is not sufficient to predict the observed changes in water temperature along the river
544 course.

545 To assess the consistency and robustness of these results, further studies could be conducted
546 using more sophisticated modeling of both the groundwater discharge and stream temperature.

547

548 **Acknowledgements**

549 This work was part of the scientific program “Control factors of river temperature at regional
550 scale in the Loire catchment” funded by European funds for regional development,
551 Etablissement Public Loire and the Loire River Basin authority (Agence de l’Eau Loire
552 Bretagne). The calculation of groundwater fluxes using groundwater budget was also funded
553 by Electricité De France (EDF) and monitored by Mohamed Krimissa from EDF.

554 We would like to thank Alain Poirel from EDF for the hourly Loire River temperature
555 measurements on the days images were taken. We would also like to thank Météo France for
556 the information from the SAFRAN database. Finally, we are very grateful to the water
557 assessment and evaluation team of the BRGM water department, particularly Alexandre
558 Brugeron, for their help in characterizing groundwater catchment areas and groundwater fluxes.

559 **References**

- 560 Alberic, P.: River backflooding into a karst resurgence (Loiret, France). *Journal of Hydrology*,
561 286, 194-202, 2004.
- 562 Alberic, P. and Lepiller, M.: Oxydation de la matière organique dans un système hydrologique
563 karstique alimenté par des pertes fluviales (Loiret, France), *Water Resources*, 32, 2051-2064,
564 1998.
- 565 Barsi, J.A., Barker, J.L., and Schott, J.R.: An atmospheric correction parameter calculator for a
566 single thermal band earth-sensing instrument, in: *Geoscience and Remote Sensing Symposium*,
567 *IGARSS'03, Proceedings, IEEE International*, 21-25 July, Toulouse, 3014-3016, 2003.
- 568 Belknap, W. and Naiman, R.J.: A GIS and TIR procedure to detect and map wall-base channels
569 in Western Washington, *Journal of Environmental Management*, 52, 147-160, 1998.
- 570 Binet, S., Auterives, C., and Charlier, J.B.: Construction d'un modèle hydrogéologique d'étiage
571 sur le val d'Orléans, rapport final, ICERE, Orléans, France, 2011.
- 572 Boyd, M. and Kasper, B.: *Analytical Methods for Dynamic Open Channel Heat and Mass*
573 *Transfer: Methodology for Heat Source Model Version 7.0*, Watershed Sciences Inc., Portland,
574 Oregon, USA, 2003.
- 575 Burkholder, B.K., Grant, G.E., Haggerty, R., Khangaonkar, T., and Wampler, P.J.: Influence
576 of hyporheic flow and geomorphology on temperature of a large, gravel bed river, Clackamas
577 River, Oregon, USA. *Hydrological Processes*, 22, 941-953, 2007.
- 578 Bustillo, V., Moatar, F., Ducharne, A., Thiery, D., and Poirel, A.: A multimodel comparison
579 for assessing water temperatures under changing climate conditions via the equilibrium
580 temperature concept: case study of the Middle Loire River, France, *Hydrological Processes*, 28,
581 1507-1524, 2014.

582 Caissie, D.: The thermal regime of rivers: a review. *Freshwater Biology*, 51, 1389-1406, 2006.

583 Cardenas, B., Harvey, J.W., Packman, A.I., and Scott, D.T.: Ground-based thermography of
584 fluvial systems at low and high discharge reveals potential complex thermal heterogeneity
585 driven by flow variation and bio-roughness, *Hydrological Processes*, 22, 980-986, 2008.

586 Casado, A., Hannah, D.M., Peiry, J.L., and Campo, A.M.: Influence of dam-induced
587 hydrological regulation on summer water temperature: Sauce Grande River, Argentina,
588 *Ecohydrology*, 6, 523-535, 2013.

589 Chander, G., Markham, B.L., and Helder, D.L.: Summary of current radiometric calibration
590 coefficients for Landsat MSS, TM, ETM+ and EO-1 ALI sensors, *Remote Sensing of*
591 *Environment*, 113, 893-903, 2009.

592 Chapra, S.C.: *Surface Water-Quality Modeling*, Civil Engineering Series, McGraw-Hill
593 International editions, Singapore, 1997.

594 Cherkauer, K.A., Burges, S.J., Handcock, R.N., Kay, J.E., Kampf, S.K., and Gillepsie, A.R.:
595 Assessing satellite based and aircraft based thermal infrared remote sensing for monitoring
596 pacific northwest river temperature, *Journal of the American Water Resources Association*, 41,
597 Issue 5, 1149-1159, 2005.

598 Chow, V.T.: *Open Channel Hydraulics*, McGraw Hill Company Inc., New York, 1959.

599 Cristea, N.C. and Burges, S.J.: Use of thermal infrared imagery to complement monitoring and
600 modeling of spatial stream temperatures, *Journal of Hydrologic Engineering*, 14, 1080-1090,
601 2009.

602 Danielescu, S., MacQuarrie, K.T.B., and Faux, N.R.: The integration of thermal infrared
603 imaging, discharge measurements and numerical simulation to quantify the relative

604 contributions of freshwater inflows to small estuaries in Atlantic Canada, *Hydrological*
605 *Processes*, 23, 2847-2859, 2009.

606 De Boer, T.: Assessing the accuracy of water temperature determination and monitoring of
607 inland surface waters using Landsat 7 ETM+ thermal infrared images, Master thesis, Delft
608 University, Netherlands, 2014.

609 Desprez, N. and Martin, C.: Inventaire des points d'eau - piézométrie et bathymétrie des
610 alluvions du lit majeur de la Loire entre Saint-Hilaire Saint-Mesmin et Saint-Laurent des Eaux,
611 BRGM, Orléans, France, Rep. 76 SGN 461 BDP, 1976.

612 Etchevers, P., Golaz, C., and Habets, F.: Simulation of the water budget and the river flows of
613 the Rhone basin from 1981 to 1994, *Journal of Hydrology*, 244, 60-85, 2001.

614 Evans, E.C., McGregor, G.R., and Petts, G.E.: River energy budgets with special reference to
615 river bed processes, *Hydrological Processes*, 12, 575-595, 1998.

616 Flipo, N., Monteil, C., Poulin, M., De Fouquet, C., and Krimissa, M.: Hybrid fitting of a
617 hydrosystem model: Long-term insight into the Beauce aquifer functioning (France), *Water*
618 *Resources Research*, 48, W05509, doi:10.1029/2011WR011092, 2012.

619 Gonzalez, R.: Étude de l'organisation et évaluation des échanges entre la Loire moyenne et
620 l'aquifère des calcaires de Beauce, Ph.D. thesis, Université d'Orléans, Orléans, France, 1991.

621 Gutierrez, A. and Binet, S.: La Loire souterraine: circulations karstiques dans le val d'Orléans,
622 *Géosciences*, 12, 42-53, 2010.

623 Habets, F., Etchevers, P., Golaz, C., Leblois, E., Ledoux, E., Martin, E., Noilhan, J., and Ottlé,
624 C.: Simulation of the water budget and the river flows of the Rhône basin, *Journal of*
625 *Geophysical Research*, 104, 31145-31172, 1999.

626 Hancock, R.N., Gillepsie, A.R., Cherkauer, K.A., Kay, J.E., Burges, S.J., and Kampf, S.K.:
627 Accuracy and uncertainty of thermal-infrared remote sensing of stream temperatures at multiple
628 spatial scales, *Remote Sensing of Environment*, 100, 427-440, 2006.

629 Hancock, R.N., Torgersen, C.E., Cherkauer, K.A., Gillepsie, A.R., Tockner, K., Faux, R.N.,
630 and Tan, J.: Thermal infrared sensing of water temperature in riverine landscapes, *Fluvial*
631 *Remote Sensing for Science and Management*, First Edition. Carbonneau P.E. and Piégay H.
632 (Eds.), John Wiley & Sons, Ltd., Chichester, 2012.

633 Hannah, D.M., Malcolm, I.A., Soulsby, C., and Youngson, A.F.: Heat exchanges and
634 temperatures within a salmon spawning stream in the Cairngorms, Scotland: Seasonal and sub-
635 seasonal dynamics, *River Research and Applications*, 20, 635-652, 2004.

636 Hannah, D.M., Malcolm, I.A., Soulsby, C., and Youngson, A.F.: A comparison of forest and
637 moorland stream microclimate, heat exchanges and thermal dynamics, *Hydrological Processes*,
638 22, 919-940, 2008.

639 Kay, J.E., Kampf, S.K., Hancock, R.N., Cherkauer, K.A., Gillepsie, A.R., and Burges, S.J.:
640 Accuracy of lake and stream temperatures estimated from thermal infrared images, *Journal of*
641 *the American Water Resources Association*, 41, 1161-1175, 2005.

642 Lamaro, A.A., Marinelarena, A., Torrusio, S.E., and Sala, S.E.: Water surface temperature
643 estimation from Landsat 7 ETM+ thermal infrared data using the generalized single-channel
644 method: Case study of Embalse del Rio Tercero (Cordoba, Argentina), *Advances in Space*
645 *Research*, 51, 492-500, 2013.

646 Latapie, A., Camenen, B., Rodrigues, S., Paquier, A., Bouchard, J.P., and Moatar, F.: Assessing
647 channel response of a long river influenced by human disturbance, *Catena*, 121, 1-12, 2014.

648 Ledoux, E., Gomez, E., Monget, J., Viavattene, C., Viennot, P., Ducharne, A., Benoit, M.,
649 Mignolet, C., Schott, C., and Mary, B.: Agriculture and groundwater nitrate contamination on
650 the Seine basin. The STICS-MODCOU modelling chain, *Sciences of Total Environment*, 33-
651 47, 2007.

652 Loheide, S.P. and Gorelick, S.M.: Quantifying stream-aquifer interactions through the analysis
653 of remotely sensed thermographic profiles and in-situ temperature histories, *Environmental*
654 *Science and Technology*, 40, 3336-3341, 2006.

655 Mallast, U., Cloaguen, R., Friesen, J., Rödiger, T., Geyer, S., Merz, R., and Siebert, C.: How to
656 identify groundwater-caused thermal anomalies in lakes based on multi-temporal satellite data
657 in semi-arid regions, *Hydrology and Earth System Sciences*, 18, 2773-2787, 2014.

658 Moatar, F. and Gailhard, J.: Water temperature behaviour in the river Loire since 1976 and
659 1881, *Surface Geosciences*, 338, 319-328, 2006.

660 Monk, W.A., Wilbur, N.M., Curry, R.A., Gagnon, R., and Faux, R.N.: Linking landscape
661 variables to cold water refugia in rivers, *Journal of Environmental Management*, 1, 170-176,
662 2013.

663 Monteil, C.: Estimation de la contribution des principaux aquifères du bassin versant de la Loire
664 au fonctionnement hydrologique du fleuve à l'étiage, Ph.D. thesis, Mines Paris Tech, Paris,
665 France, 2011.

666 Pryet, A., Labarthe, B., Saleh, F., Akopian, M., and Flipo, N.: Reporting of stream-aquifer flow
667 distribution at the regional scale with a distributed process-based model, *Water Resources*
668 *Management*, 29, 139-159, 2015.

669 Quintana-Segui, P., Moigne P.L., Durand Y., Martin E., Habets, F., Baillon, M., Canellas, C.,
670 Franchisteguy, L., and Morel, S.: Analysis of near surface atmospheric variables: Validation of

671 the SAFRAN analysis over France, *Journal of Applied Meteorology and Climatology*, 47, 92-
672 107, 2008.

673 Robinson, I.S., Wells, N.C., and Charnock, H.: The sea surface thermal boundary layer and its
674 relevance to the measurements of sea surface temperature by airborne and spaceborne
675 radiometers, *International Journal of Remote Sensing*, 5, 19-45, 1984.

676 Rushton, K.: Representation in regional models of saturated river-aquifer interaction for
677 gaining-losing rivers, *Journal of Hydrology*, 334, 262-281, 2007.

678 Saleh, F., Flipo, N., Habets, F., Ducharme, A., Oudin, L., Viennot, P., Ledoux, E.: Modeling the
679 impact of in-stream water level fluctuations on stream-aquifer interactions at the regional scale,
680 *Journal of Hydrology*, 400, 490-500, 2011.

681 Salencon, M.J. and Thébault, J.M.: *Modélisation d'écosystème lacustre*, Masson (Eds.), Paris,
682 France, 1997.

683 Schomburgk, S., Brugeron, A., Winckel, A., Ruppert, N., Salquebre D., and Martin, J.C.:
684 Contribution des principaux aquifères au fonctionnement hydrologique de la Loire en région
685 Centre – Caractérisation et bilans par bassins versants souterrains, BRGM, Orléans, France,
686 Rep. BRGM/RP 60381-FR, 2012.

687 Smikrud, K.M., Prakash, A., and Nichols, J.V.: Decision-based fusion for improved fluvial
688 landscape classification using digital aerial photographs and forward looking infrared images,
689 *Photogrammetry and Remote Sensing*, 74, 903-911, 2008.

690 Sophocleous, M.: Interactions between groundwater and surface water: the state of science,
691 *Hydrogeology Journal*, 10, 52-67, 2002.

692 Tonolla, D., Acuna, V., Uehlinger, U., Frank, T., and Tockner, K.: Thermal heterogeneity in
693 river floodplains, *Ecosystems*, 13, 727-740, 2010.

694 Torgersen, C.E., Price, D.M., Li, H.W., and McIntosh, B.A.: Multiscale thermal refugia and
695 stream habitat associations of Chinook salmon in northeastern Oregon, *Ecological*
696 *Applications*, 9, 301-319, 1999.

697 Torgersen, C.E., Faux, R.N., McIntosh, B.A., Poage, N.J., and Norton, D.J.: Airborne thermal
698 remote sensing for water temperature assessment in rivers and streams, *Remote Sensing of*
699 *Environment*, 76, 386-398, 2001.

700 US Geological Survey: Landsat-A Global Land-Imaging Mission, US Geological Survey Fact
701 sheet, Sioux Falls, Dakota, USA, p. 4, 2012, revised: 30 May 2013.

702 Wang, L.T., McKenna, T.E., and DeLiberty, T.L.: Locating ground-water discharge areas in
703 Rehoboth and Indian River bays and Indian River, Delaware, using Landsat 7 imagery, Report
704 of investigation no. 74, Delaware geological survey, Newark, State of Delaware, USA, 2008.

705 Ward, J.V.: *Aquatic Insect Ecology, Part I, biology and habitat*, Wiley & Son (Eds.), New York,
706 USA, 1992.

707 Wawrzyniak, V.: *Etude multi-échelle de la température de surface des cours d'eau par imagerie*
708 *infrarouge thermique: exemples dans le bassin du Rhône*, Ph.D. thesis, Université Jean-Moulin,
709 Lyon, France, 2012.

710 Wawrzyniak, V., Piégay, H., and Poirel, A.: Longitudinal and temporal thermal patterns of the
711 French Rhône River using Landsat ETM+ thermal infrared (TIR) images, *Aquatic Sciences*,
712 74, 405-414, 2012.

713 Wawrzyniak, V., Piégay, H., Allemand, P., Vaudor, L., and Grandjean, P.: Prediction of water
714 temperature heterogeneity of braided rivers using very high resolution thermal infrared (TIR)
715 images, *International Journal of Remote Sensing*, 34, 4812-4831, 2013.

- 716 Webb, B.W. and Zhang, Y.: Spatial and seasonal variability in the components of the river heat
717 budget, *Hydrological Processes*, 11, 79-101, 1997.
- 718 Webb, B.W. and Zhang, Y.: Water temperatures and heat budgets in Dorset chalk water courses,
719 *Hydrological Processes*, 13, 309-321, 1999.

720 Table 1. Loire River temperature, air temperature and river flow rate at the date and time
 721 satellite images where taken.

Date	Daily river flow in Orléans (m³.s⁻¹)	Hourly mean water temperature in Dampierre (°C)	Hourly mean water temperature in Saint-Laurent des Eaux (°C)	Hourly air temperature in Orléans (°C)
Winter				
15/11/2001	182	5.2	5.8	5.6
22/02/2003	478	4.2	5.5	12.7
Summer				
29/05/2003	89	22.8	20.1	25.5
19/07/2010	112	23.4	23.1	28.3
20/08/2010	78	21.8	20.9	28.3
24/08/2000	83	24.0	22.5	30.4
29/07/2002	61	28.3	26.0	32.5

722

723 Table 2. Details of the atmospheric heat flux calculations.

Solar radiation	RS estimated from the SAFRAN database	
Atmospheric radiation	$RA = \sigma \cdot (T_a + 273.15)^4 \cdot (A + 0.031 \cdot \sqrt{e_a}) \cdot (1 - R_L)$	<p>T_a (°C) is the air temperature estimated from the SAFRAN database from Météo France</p> <p>$\sigma = 4.9 * 10^{-3} J \cdot m^{-2} \cdot d^{-1} \cdot K^{-4}$ is the Stefan-Boltzman constant</p> <p>$A = 0.6$ $R_L = 0.03$ are attenuation and reflection coefficients</p> <p>$e_a = 1.22 * Q_a$ is the air vapour pressure</p> <p>Q_a in $g \cdot kg^{-1}$ is the specific humidity of air estimated from the SAFRAN database</p>
Emitted radiation	$RE = \varepsilon \cdot \sigma \cdot (T_w + 273.15)^4$	<p>$\varepsilon = 0.98$ is the water emissivity</p> <p>T_w (°C) is the mean water temperature on the section estimated from the longitudinal temperature profiles</p>
Conduction	$CV = \rho_a \cdot C_a \cdot e(V) \cdot (T_w - T_a)$	<p>$\rho_a = 1.293 \cdot (\frac{273.15}{T})$ air density in $kg \cdot m^{-3}$ is the function of air temperature T (K) estimated from the SAFRAN database</p> <p>$C_a = 1002 J \cdot kg^{-1} \cdot C^{\circ-1}$ is the specific heat of air</p> <p>$e(V) = 0.0025 * (1 + V_2)$ is the function of the wind 2 m above the ground V_2 ($m^3 \cdot s^{-1}$)</p> <p>$V_2 = V_{10} \cdot (\frac{2}{10})^{0.11}$ is used to estimate the wind 2 m above the ground as a function of the wind 10 m above the ground, itself estimated from the SAFRAN database</p>
Condensation / Evaporation	$CE = L(T_w) \cdot \rho_a \cdot e(V) \cdot (Q_w - Q_a)$	<p>$L(T_w) = (2500.9 - 2.365 \cdot T_w) \cdot 10^3 J \cdot kg^{-1}$ is the latent evaporation heat</p>

		$Q_w = \frac{4.596 \cdot e^{\frac{237.3 \cdot T_w}{237.3 + T_w}}}{1.22}$ <p>Q_w in $g \cdot kg^{-1}$ is the specific humidity of saturated air at the water temperature</p>
--	--	---

724

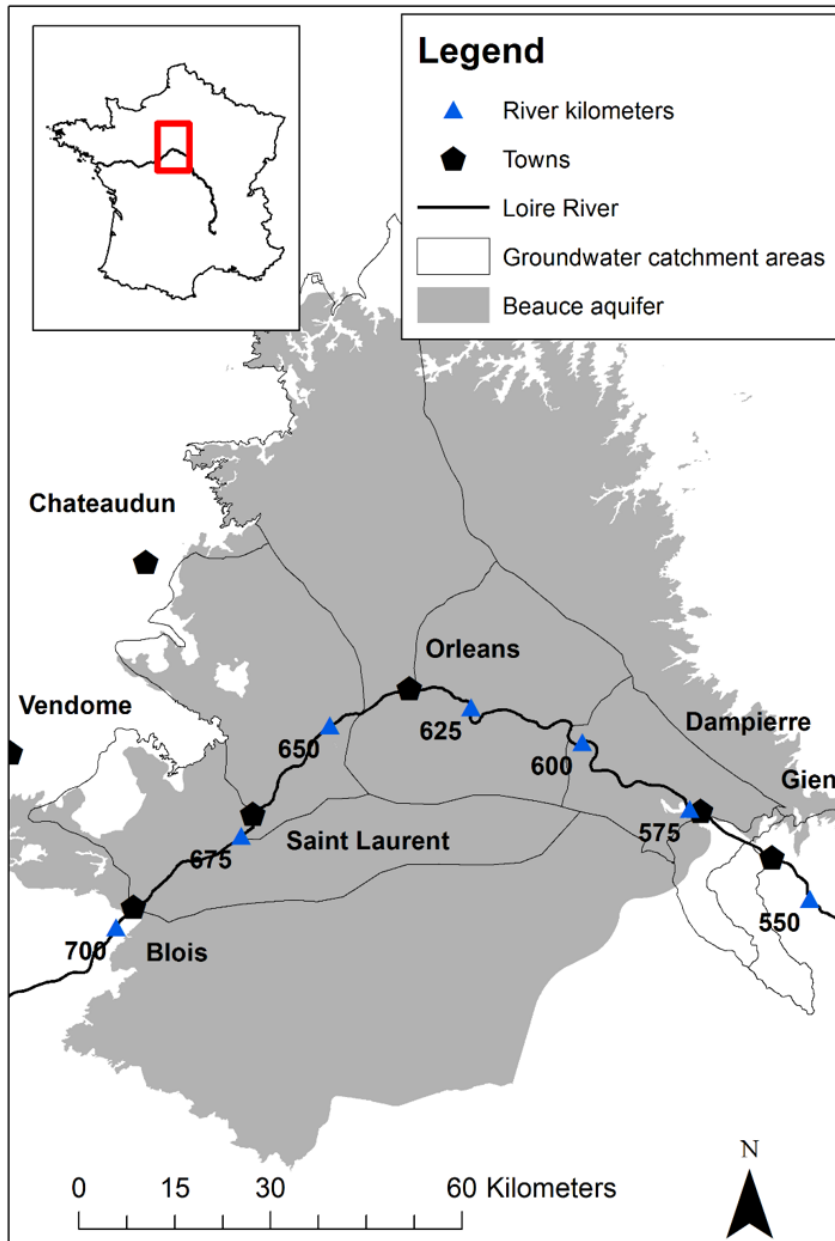
725 Table 3. Standard deviation of water temperature (°C) estimated on all the 200m sections of the
 726 Loire River. Standard deviations were calculated at sections with under 20 water pixels and
 727 over 20 water pixels.

Date	24/08/2000	15/11/2001	29/07/2002	22/02/2003	29/05/2003	19/07/2010	20/08/2010
σ (n<20)	0.70	0.56	0.76	0.32	0.45	0.42	0.52
σ (n>20)	0.50	0.44	0.73	0.26	0.41	0.41	0.42

728

729

730 Figure 1. Map of the study area. The delineation of the Beauce aquifer comes from the BDLISA
731 database from the Bureau de Recherches Géologiques et Minières (BRGM).

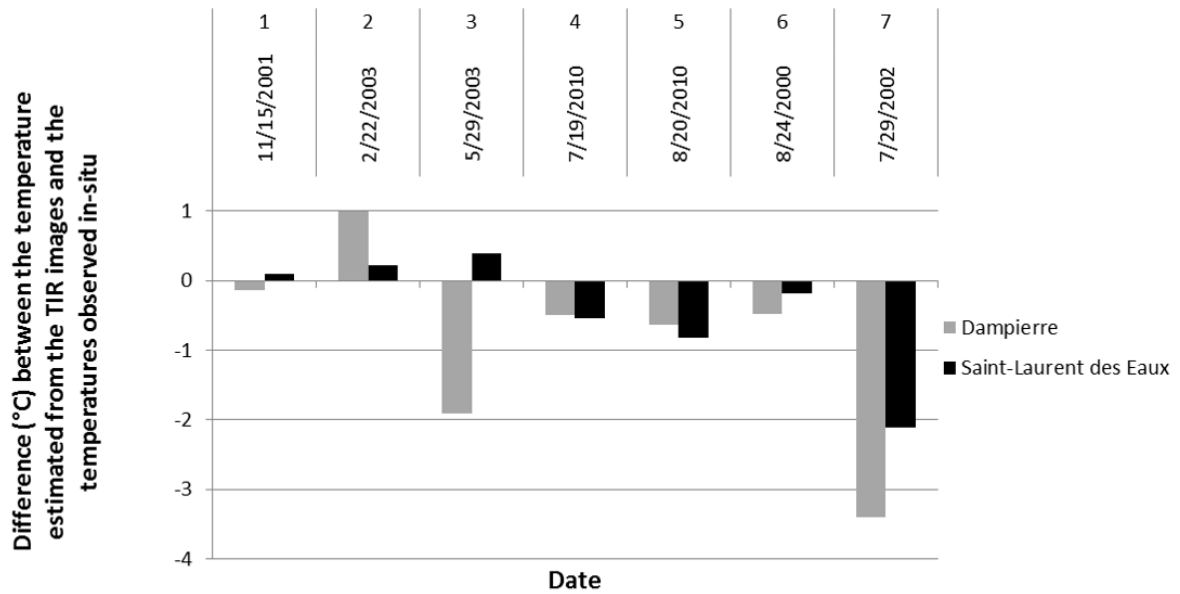


732

733

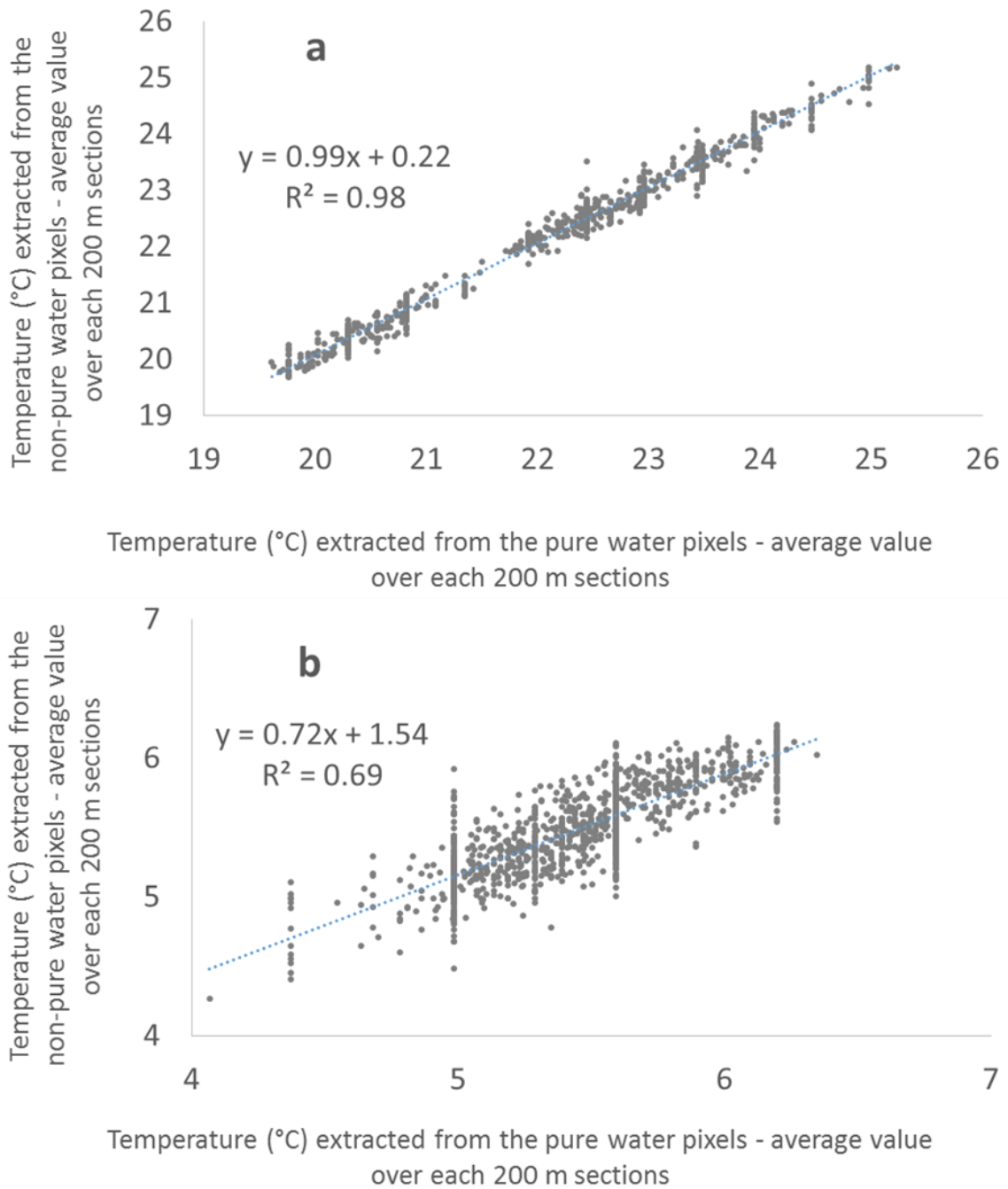
734

735 Figure 2. Differences between TIR derived temperatures extracted from the longitudinal
 736 temperature profile and *in situ* measurements (at the same date and time) for each date. The
 737 dates are classified according to the air temperature at the time when the images were taken (air
 738 temperature rose from 15/11/2001 to 29/07/2002).



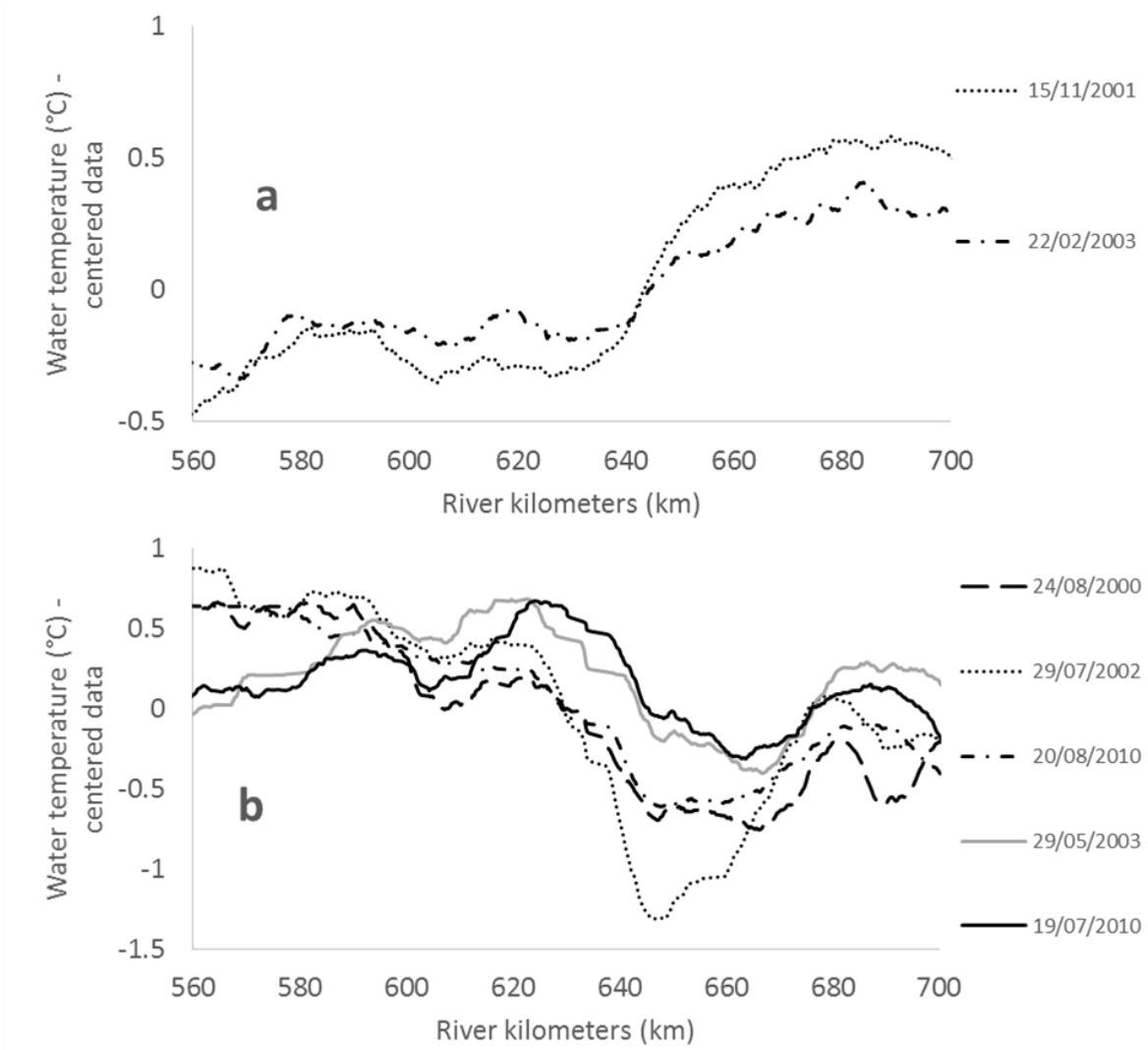
739
 740
 741

742 Figure 3. A: Relationship between the temperatures extracted from the non-pure water pixels
 743 and those from the pure water pixels. Temperature values of both pixel types were averaged
 744 over the successive 200m sections where pure water pixels existed. Summer temperatures are
 745 represented. B: Relationship between the temperatures extracted from the non-pure water pixels
 746 and from the pure water pixels. The temperatures of both pixel types were averaged over the
 747 successive 200m sections where pure water pixels existed. Winter temperatures are represented.



748

749 Figure 4. A: Loire temperature profiles in winter extracted from the TIR images. B: Loire
750 temperature profiles in summer extracted from the TIR images. For each profile data were
751 centered.

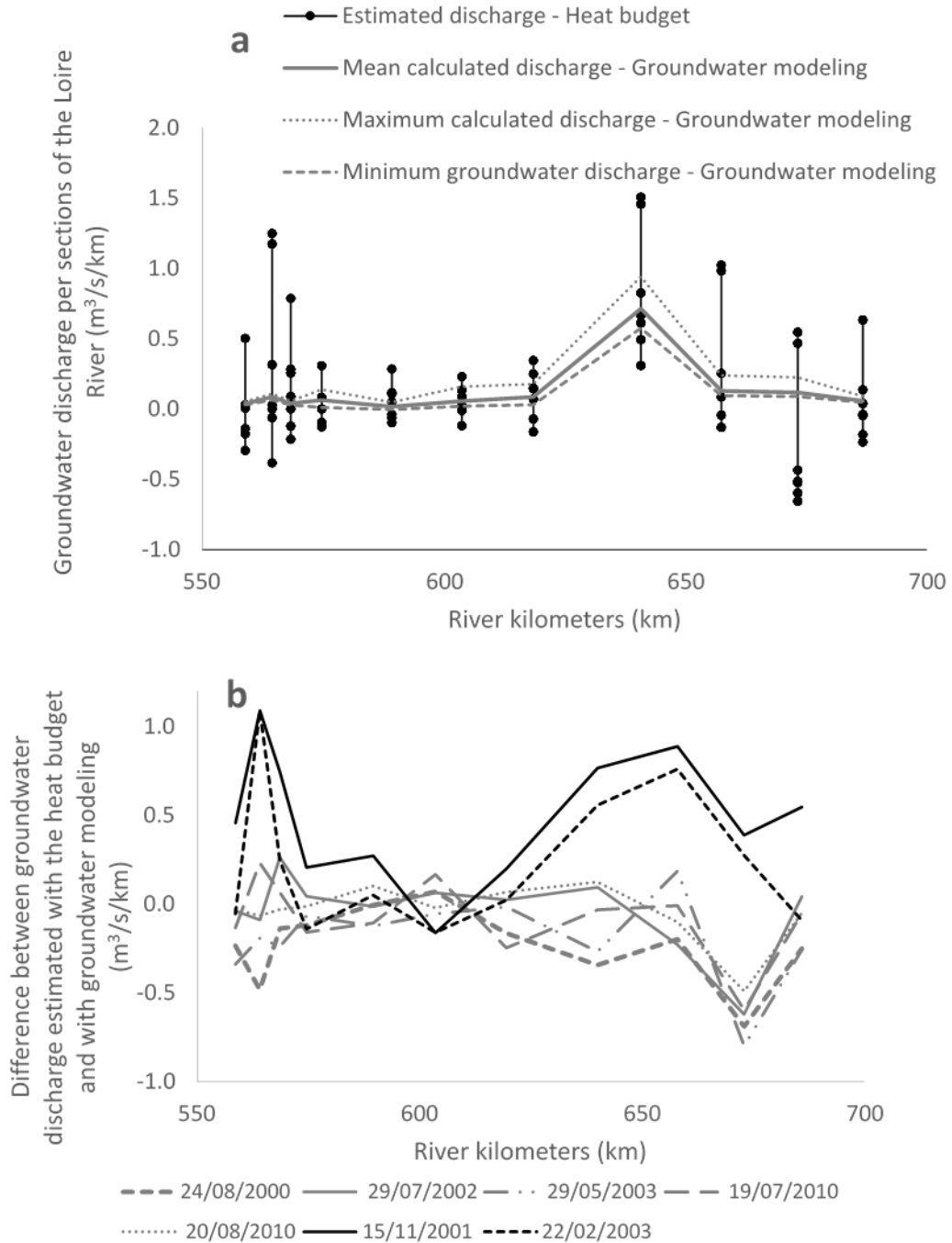


752

753

754

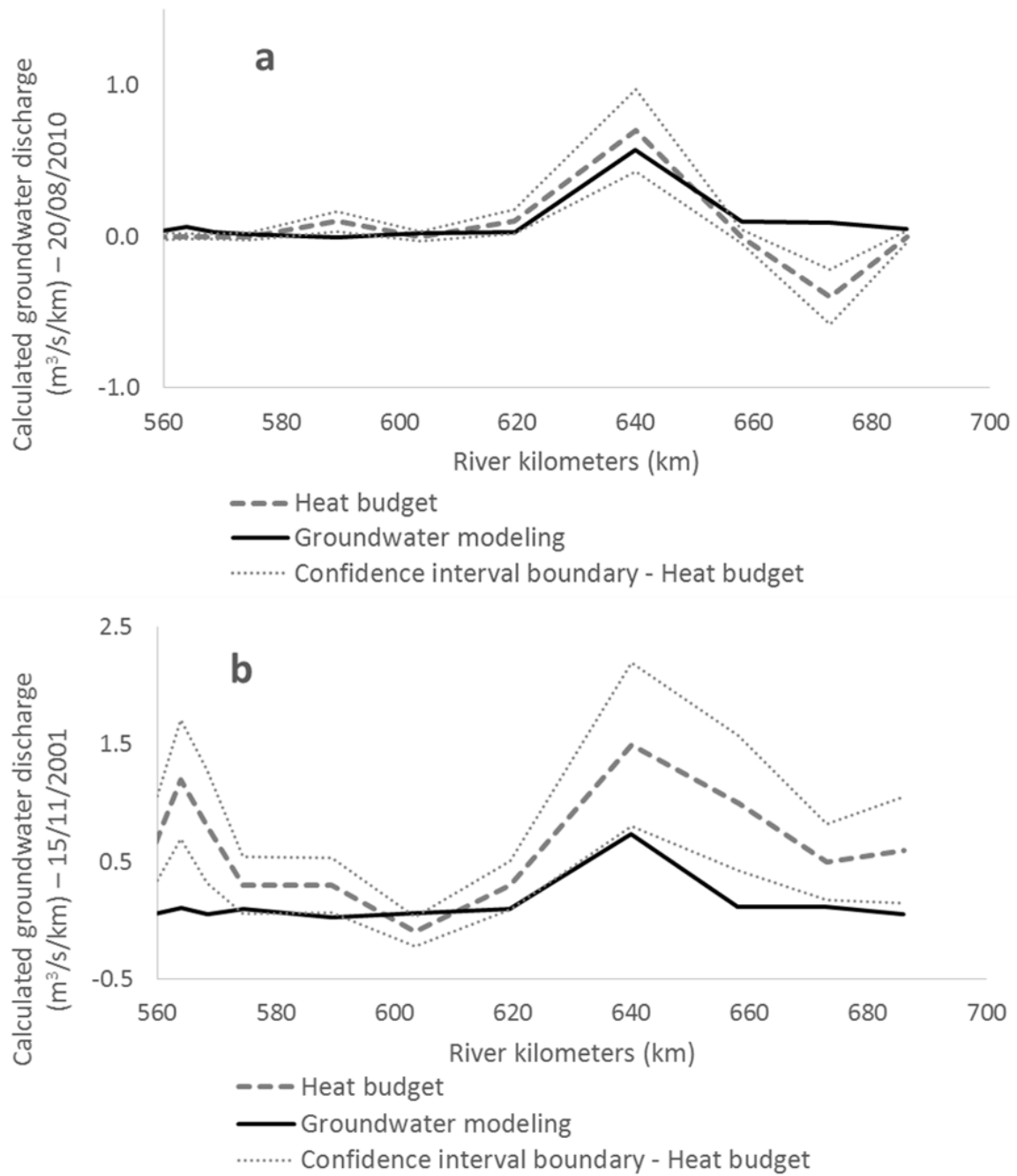
755 Figure 5. A: Groundwater discharge per section of the Loire River estimated at the different
 756 dates using the heat budget based on the TIR images (black points), and calculated by
 757 groundwater modeling (grey line), as a function of the river kilometers. B: Absolute value of
 758 the difference between groundwater discharges estimated by groundwater modeling and the
 759 heat budget.



760

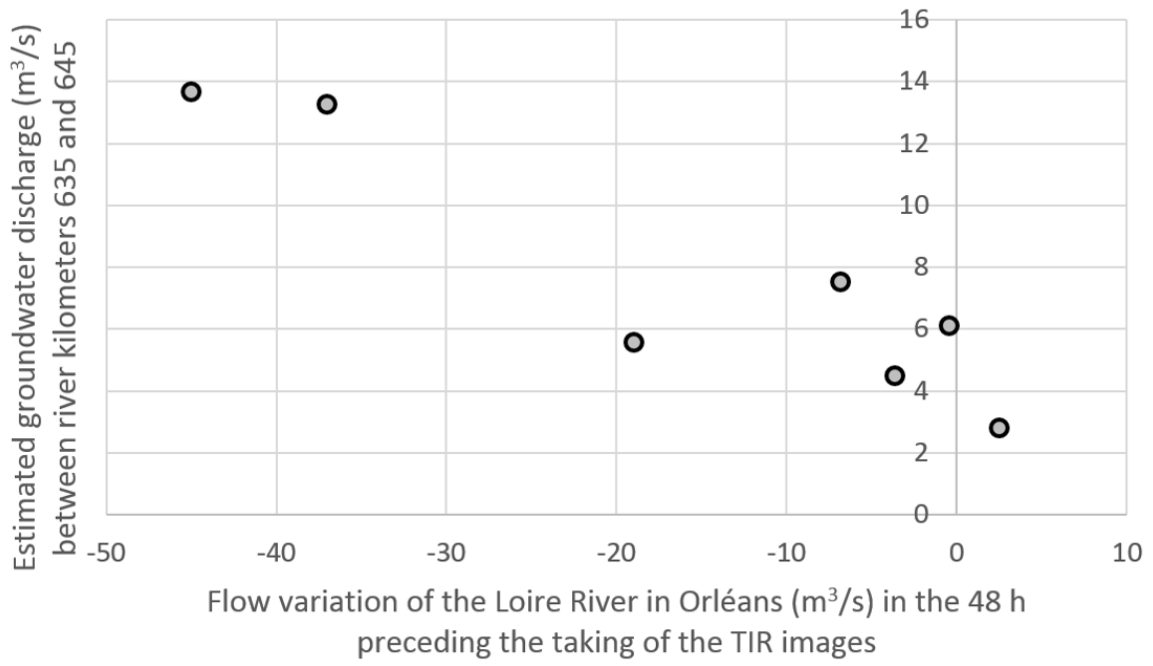
761

762 Figure 6. A: Calculated groundwater discharge along the Loire River in 20/08/2010 using
 763 groundwater modeling and the heat budget. B: Calculated groundwater discharge along the
 764 Loire River in 15/11/2001 using groundwater modeling and the heat budget.



765
 766
 767

768 Figure 7. Groundwater discharge rate as a function of the variation in river flow in the 48 h
769 before the TIR image was taken.

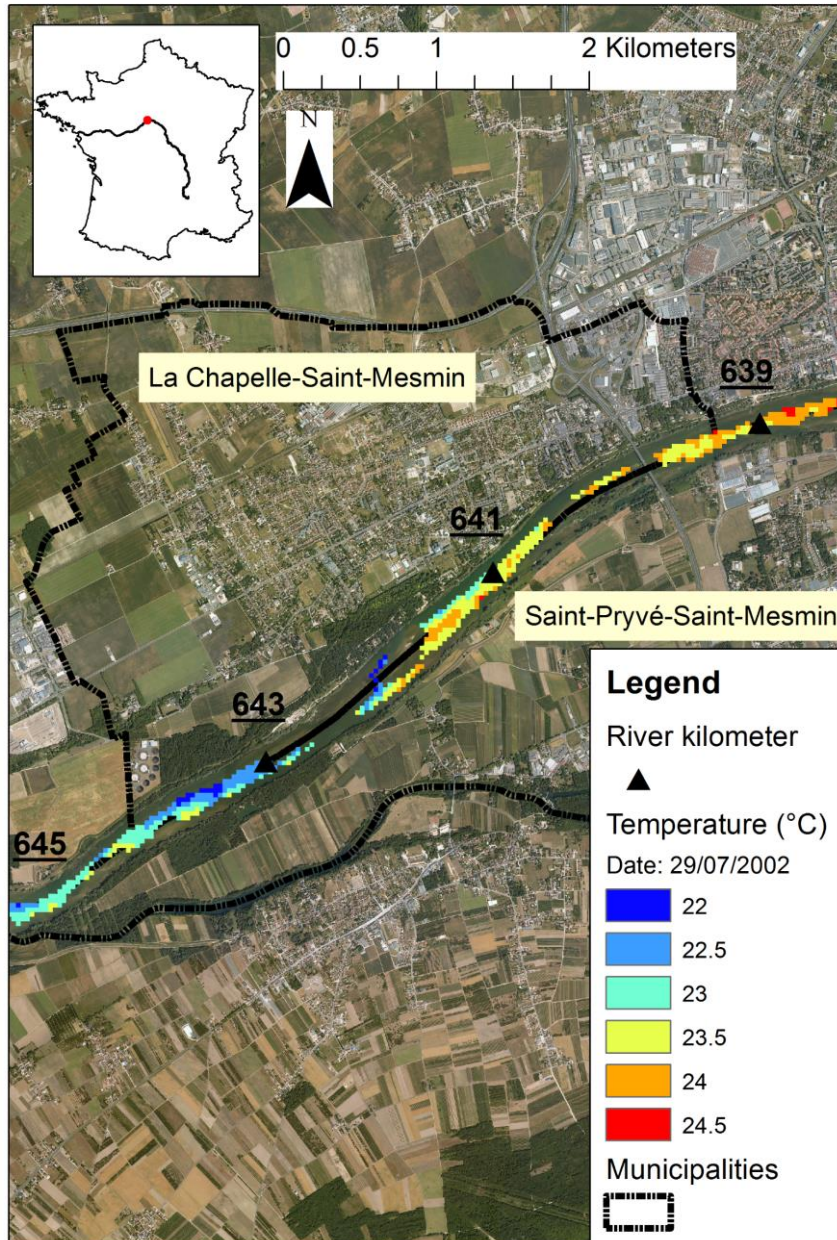


770

771

772

773 Figure 8. Temperatures measured in the Loire River in the vicinity of La Chapelle Saint-
774 Mesmin on the 29/07/2002. Groundwater discharge is visible along the right bank (north side)
775 of the Loire River as a cold patch between river kilometers 642 and 644.



776

777